

OPTIMAL MESH SIZE FOR INVERSE MEDIUM SCATTERING PROBLEMS*

HABIB AMMARI[†], YAT TIN CHOW[‡], AND KEJI LIU[§]

Abstract. An optimal mesh size of the sampling region can help to reduce computational burden in practical applications. In this work, we investigate optimal choices of mesh sizes for the identifications of medium obstacles from either the far-field or near-field data in two and three dimensions. The results would have applications in the reconstruction process of inverse scattering problems.

Key words. optimal mesh size, inclusion reconstruction, inverse medium scattering problems

AMS subject classifications. 35R30, 45Q05, 65R32

DOI. 10.1137/18M122159X

1. Introduction. The direct and inverse medium scattering problems have been investigated extensively in the past few decades due to their important practical applications in geophysics, nondestructive testing, biological studies, evaluation, and medicine (see, for instance, [2, 4, 10, 11]). A large variety of numerical reconstruction methods have been developed and applied in practice for different kinds of models. For instance, some effective methods are developed for the homogeneous background model: the linear sampling (or probing) method (LSM) [17], the time-reversal multiple signal classification method (MUSIC) [6, 7, 13], the direct sampling method (DSM) [24], the multilevel sampling method (MSM) [31], the contrast source inversion method (CSIM) [12], etc. Moreover, several efficient algorithms are applied in various practical situations, e.g., in the stratified ocean waveguide model: the simple method (SM) [28], extended direct sampling methods (EDSMs) [14, 15, 16, 25, 26, 27, 29, 30, 32, 33], the extended MUSIC method (EMUSIC) [5, 23], the topological based imaging functional [3], etc. Furthermore, several efficient approaches are introduced in the two-layered medium model: the extended multilevel sampling method (EMSM) [35], the extended linear sampling method (ELSM) [19], etc.

Most reconstruction methods involve an indicator function (called also the imaging functional) to be evaluated at each sampling point inside a sampling region for the recovery of the shape (and, if possible, the parameters therein) of the unknown inclusions. In practice, the sampling region is usually chosen to be large enough to contain all the unknown inclusions; then a considerably fine mesh is used in the sam-

*Received by the editors October 19, 2018; accepted for publication (in revised form) December 6, 2019; published electronically February 20, 2020.

<https://doi.org/10.1137/18M122159X>

Funding: The work of the first author was partially supported by Swiss National Science Foundation grant 200021-172483. The work of the second author was supported by ONR grant N000141712162 and by NSF grant DMS-1720237. The work of the third author was supported by the NNSF of China, grant 11601308, by the Science and Technology Commission of Shanghai Municipality under the “Shanghai Rising-Star Program,” grant 19QA1403400, and by the Natural Science Foundation of Shanghai, grant 18ZR1413200.

[†]Department of Mathematics, ETH Zürich, Rämistrasse 101, CH-8092 Zürich, Switzerland (habib.ammari@math.ethz.ch).

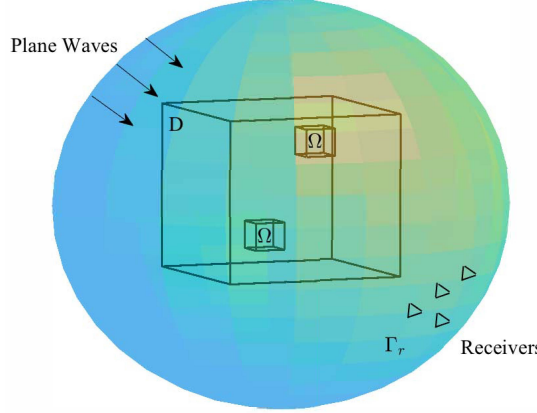
[‡]Department of Mathematics, University of California, Riverside, CA 92521 (yattinc@ucr.edu).

[§]Corresponding author. School of Mathematics, Shanghai Key Laboratory of Financial Information Technology, Shanghai University of Finance and Economics, 777 Guoding Road, Shanghai 200433, People’s Republic of China (liu.keji@sufe.edu.cn, kjliu.ip@gmail.com).

pling region to reconstruct the details of the objects. However, an extremely fine mesh would drastically increase the computational complexity in practice, especially in the three-dimensional case. In fact, the computation complexity of most reconstruction methods (see, for instance, DSM, MUSIC, LSM, CSIM, etc.) is of $\mathcal{O}(N^2)$ in two dimensions and $\mathcal{O}(N^3)$ in three dimensions, where N is the number of sampling points along one direction. Reconstruction methods such as MSM and the EMSM have complexity of order $N \log N$ in two dimensions and $N^2 \log N$ in three dimensions. Hence, they are still quite demanding if N is large. Therefore, an optimal mesh size for the sampling and the reconstruction is crucial to reduce the computation complexity of these algorithms and at the same time to reconstruct details of the inclusions in practical applications. Moreover, several iterative methods (i.e., EMSM, CSIM, etc.) apply certain cutoff values as a stopping criterion of the method. Such a choice of stopping criterion may heavily depend on the reconstruction quality under a coarser mesh and a subjective choice of the cutoff value, which sometimes causes the reconstruction algorithm to entirely miss some small inclusions. Choosing an optimal mesh size can improve the quality of the reconstruction and practically avoid the aforementioned issue.

To the best of the authors' knowledge, although there are quite a lot of discussions of resolution analysis (e.g., Abbe-Rayleigh resolution limit, Sparrow's resolution limit, etc.) in inverse scattering problems, e.g., [1, 8, 20, 22], a systematic choice of the optimal mesh size for numerical reconstruction algorithms in inverse scattering problems has not yet been addressed in the literature. We would like to remark that the resolution analysis aims at understanding the quality of an image given a fixed grid size, whereas here we aim at choosing an optimal mesh size to ensure a certain quality of the reconstruction. This paper is hence devoted to an optimal selection of the mesh size in reconstruction methods. It is worth emphasizing that, in this paper, instead of focusing on one particular reconstruction method, we are interested in an optimal choice of the mesh size in a numerical reconstruction scheme assuming a maximal resolving power. We shall provide an optimal selection of mesh size for the identifications of unknown inclusions from both the far-field and the near-field data in two and three dimensions. Using our optimal mesh-size, the order of computational complexity of the aforementioned methods (e.g., DSM, MUSIC, LSM, CSIM, etc.) would be improved to $\mathcal{O}(N_{\text{opt}}^2)$ in two dimensions and $\mathcal{O}(N_{\text{opt}}^3)$ in three dimensions, where N_{opt} is the number of points of a chosen optimal mesh along one dimension. Similarly, reconstruction methods such as MSM and the EMSM would have their complexity order improved to an order of $N_{\text{opt}} \log N_{\text{opt}}$ in two dimensions and $N_{\text{opt}}^2 \log N_{\text{opt}}$ in three dimensions. In our paper, we obtain an optimal mesh-size that would provide us N_{opt} , which can be readily obtained by integrating the density of the optimal mesh over the domain. This choice is optimal in a sense that a further refinement of N will not improve image quantity and therefore the increased computational effort would be unnecessary and wasted.

This paper is organized as follows. In section 2, we state the forward problems that we focus on. We then provide in section 3 an optimal mesh size selection given far-field data, whereas in section 4, we consider the mesh size problem when near-field data are available. In section 5.1, we describe how our optimal mesh size function may help to refine our mesh in order to resolve clustered inclusions. In section 5, we show that our choice of mesh size is indeed optimal by comparing several reconstructions from a typical numerical method with different mesh sizes. Finally, some concluding remarks are presented in section 6. The results of this paper can help minimizing the computation complexity of methods designed for solving inverse scattering prob-

FIG. 1. *Plane wave illumination.*

lems. A similar analysis can be performed for electromagnetic and elastic inverse wave scattering problems.

2. Problem description. In this section, we shall describe the direct and inverse scattering problems in the presence of inhomogeneous inclusions (inside a sampling domain Ω ; see Figure 1) embedded in a homogeneous background medium $\mathbb{R}^M (M \geq 2)$. Consider an inhomogeneous inclusion represented by a (variable) contrast $q \in L^\infty(\mathbb{R}^M)$ such that $\text{supp}(q) \subset \Omega$, i.e., it vanishes outside Ω .

2.1. Forward problem. We are now ready to state the considered forward problems. For numerical simulations of solutions of these forward problems, we refer the reader, for instance, to [31, 33].

2.1.1. Plane wave illumination. Suppose that u^i is an incident plane given by

$$u^i(x, d_y) := e^{ik d_y \cdot x},$$

where $d_y \in \mathbb{S}^M$ is the direction of incidence with k being the wave number and \mathbb{S}^M being the unit sphere in \mathbb{R}^M . Then, u^i satisfies the Helmholtz equation

$$\Delta u^i + k^2 u^i = 0 \quad \text{for } x \in \mathbb{R}^M.$$

We now consider the total field u as the solution to the following equation,

$$(2.1) \quad \Delta u + k^2 (1 + q(x)) u = 0 \quad \text{for } x \in \mathbb{R}^M,$$

subject to the outgoing Sommerfeld radiation condition,

$$(2.2) \quad \frac{\partial u^s}{\partial r} - iku^s = o\left(\frac{1}{r^{(M-1)/2}}\right) \quad \text{as } r \rightarrow \infty,$$

which holds uniformly in all directions $x/|x|$, where $r = |x|$ and $u^s := u - u^i$ is the scattered field.

From (2.1), due to the presence of inclusions in Ω , the Lippmann–Schwinger representation formula of the total field u yields

$$(2.3) \quad u^s(x, d_y) = u(x, d_y) - u^i(x, d_y) = k^2 \int_{\Omega} q(z) G(x, z) u(z, d_y) dz, \quad d_y \in \mathbb{S}^M,$$

where $G(x, z), x, z \in \mathbb{R}^M$ and $x \neq z$ is the Green function associated with the homogeneous background,

$$(2.4) \quad G(x, z) = C_M k^{\frac{2-M}{2}} |x - z|^{\frac{2-M}{2}} H_{\frac{M-2}{2}}^{(1)}(k|x - z|).$$

Here, $H_\nu^{(1)}$ is the Hankel function of the first kind of order ν and $C_M = -i(2\pi)^{\frac{2-M}{2}}/4$. In particular, we have

$$(2.5) \quad G(x, z) = \begin{cases} \frac{i}{4} H_0^{(1)}(k|x - z|) & \text{for } M = 2, \\ \frac{e^{ik|x-z|}}{4\pi|x-z|} & \text{for } M = 3. \end{cases}$$

2.1.2. Point source illumination. On the other hand, suppose that u^i is generated from a point source $y \in \Gamma_s$, where Γ_s is a surface. Then,

$$u^i(x, y) := G(x, y) = C_M k^{\frac{2-M}{2}} |x - z|^{\frac{2-M}{2}} H_{\frac{M-2}{2}}^{(1)}(|x - y|),$$

which now satisfies

$$\Delta u^i + k^2 u^i = \delta_y \quad \text{for } x \in \mathbb{R}^M.$$

Consider the total field u as the solution to the following equation:

$$(2.6) \quad \Delta u + k^2 (1 + q(x)) u = \delta_y \quad \text{for } x \in \mathbb{R}^M$$

with $u^s := u - u^i$ satisfying the outgoing Sommerfeld radiation condition (2.2).

From (2.6), due to the presence of inclusions in Ω , the total field u satisfies the following equation:

$$(2.7) \quad u(x, y) = u^i(x, y) + k^2 \int_{\Omega} q(z) G(x, z) u(z, y) dz, \quad x \in \mathbb{R}^M \text{ and } y \in \Gamma_s.$$

Because the corresponding scattered field u^s is measured by the receivers on the surface Γ_r , it has the following representation:

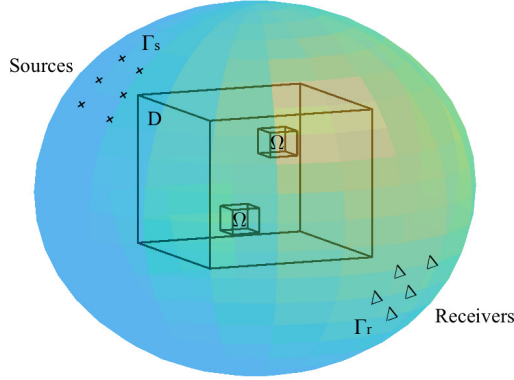
$$(2.8) \quad u^s(x, y) = k^2 \int_{\Omega} q(z) G(x, z) u(z, y) dz, \quad x \in \mathbb{R}^M \text{ and } y \in \Gamma_s.$$

We refer to Figure 2 for a schematic configuration of the inverse medium scattering problem. We may again consider measurements $u(x, y)$ along a surface $x \in \Gamma_r$ where $y \in \Gamma_s$.

2.2. Inverse problem. The inverse problem of our interest is to recover the physical features of the inclusions inside Ω from knowledge of the scattered field u^s .

For plane wave illuminations, we consider the following problem: given the measurements of $u^s(x, d_y)$ along a surface $x \in \Gamma_r$, where the distance $\text{dist}(\Gamma_r, \Omega) \gg 1$, and $d_y \in \mathbb{S}^M$, where u satisfies (2.3), we aim at recovering $q(x), x \in \Omega$.

In the case of point source illuminations, we consider the following problem: given the measurements of $u^s(x, y)$ along a surface $x \in \Gamma_r$ and $y \in \Gamma_s$, where u satisfies (2.7), we aim at recovering $q(x), x \in \Omega$.

FIG. 2. *Point source illumination.*

Note that there are many numerical methods addressing the number of required directions of incidence (see, for instance, [12, 13, 17, 33, 32]). Since our work does not focus on any particular type of reconstruction methods, but aims at discussing how to choose the mesh size in general, we do not advocate any particular choice of numerical reconstruction methods. Nevertheless, in this subsection, for the sake of completeness, we state two examples of indicator functions in order to illustrate our main ideas. In what follows, we provide a brief description of two types of indicator functions: index functions provided in the MSM [28, 29, 31] and the DSM (see, for instance, [24, 28, 33]). Both methods work either with plane wave or point source illuminations; nonetheless, for the sake of simplicity, we only consider the case of plane wave illuminations.

Example 1. We would like to briefly describe the index function shown in the MSM. Given a choice of sampling points $x \in \Omega$, consider an incident direction $d_y \in \mathbb{S}^{M-1}$. We first introduce the contrast source function ϕ , which is defined as follows:

$$\phi(x, d_y) := k^2 q(x) u(x, d_y) \quad \text{for } x \in \Omega.$$

The scattered field u^s can thus be expressed into the following compact form:

$$u^s(x_r, d_y) = \mathcal{P}_r \phi(x_r, d_y) \quad \text{for } x_r \in \Gamma_r,$$

where the integral operator \mathcal{P}_r is given, for $x_r \in \Gamma_r$, by

$$\mathcal{P}_r \phi(x_r, d_y) := \int_{\Omega} G(x, x_r) \phi(x, d_y) dx.$$

The MSM aims at approximating the contrast source function at sampling points $x \in \Omega$ given by a mesh with multiple choices of d_y via a backpropagation method, and then refine the choices of mesh sizes in order to obtain iteratively another set of $x \in \Omega$. A backpropagation $\phi_b(\cdot, d_y)$, which is defined as follows, is employed to provide an (initial) approximation of $\phi(x, d_y)$:

$$\phi_b := \frac{\|\mathcal{P}_r^* u^s\|_{L^2(\Omega)}^2}{\|\mathcal{P}_r \mathcal{P}_r^* u^s\|_{L^2(\Gamma_r)}^2} \mathcal{P}_r^* u^s.$$

Here, \mathcal{P}_r^* is known as the backpropagation operator which is represented as

$$\mathcal{P}_r^* \phi(x; d_y) := \int_{\Gamma_r} \overline{G(\xi; x)} \phi(\xi; d_y) d\sigma_\xi \quad \text{for } x \in \Omega.$$

In practice, the expression of contrast source function is numerically obtained by

$$(2.9) \quad \tilde{\phi}_{b,n}(x) := \frac{\|\mathcal{P}_r^* u^s(\cdot, d_{y,n})\|_{L^2(\Omega)}^2}{\|\mathcal{P}_r \mathcal{P}_r^* u^s(\cdot, d_{y,n})\|_{L^2(\Gamma_r)}^2} \mathcal{P}_r^* u^s(x, d_{y,n}) \quad \text{for } x \in \Omega$$

for a finite number of incidences $d_{y,n} \in \mathbb{S}^{M-1}$, where $n = 1, 2, \dots, N$. With this in hand, we now define an index function or indicator function $\eta(x)$, which aims at numerically approximating $k^2 q(x)$ from the measured values of $\{u^s(\cdot, d_{y,n})\}_{n=1}^N$, as the least-square solution to the system

$$(2.10) \quad \tilde{\phi}_{b,n} = \eta(x) u(x, d_{y_n})$$

for $n = 1, 2, \dots, N$. Here, the points $x \in \Omega$ are the chosen sampling points in Ω , and $\eta(x)$ can be explicitly given by

$$(2.11) \quad \eta(x) := \Re \left\{ \frac{\sum_{n=1}^N \tilde{\phi}_{b,n}(x) \overline{(u^i(x, d_{y,n}) + \mathcal{P}_\Omega \tilde{\phi}_{b,n})}}{\sum_{n=1}^N |u^i(x, d_{y,n}) + \mathcal{P}_\Omega \tilde{\phi}_{b,n}|^2} \right\} \quad \text{for } x \in \Omega,$$

where $\Re\{\cdot\}$ denotes the real part of a complex number, $\tilde{\phi}_{b,n}$ are defined in (2.9), and the integral operator \mathcal{P}_Ω is defined, for all $x \in \Omega$, by

$$\mathcal{P}_\Omega \phi(x, d_y) := \int_{\Omega} G(\xi, x) \phi(\xi, d_y) d\xi.$$

Now the algorithm chooses a certain threshold of cutoff to numerically identify the support of the index function or indicator function η , and then the choices of $x \in \Omega$ are resampled, and the whole process is preformed again and iterated until a fine reconstruction profile is achieved.

Example 2. Another example of indicator functions is provided by the DSM. For a given incidence $d_y \in \mathbb{S}^M$, the index function is defined by

$$(2.12) \quad I(x, d_y) := \frac{|\langle u^s(\cdot, d_y), G(\cdot, x) \rangle_{L^2(\Gamma_r)}|}{\|u^s(\cdot, d_y)\|_{L^2(\Gamma_r)} \|G(\cdot, x)\|_{L^2(\Gamma_r)}} \quad \forall x \in \Omega,$$

where the inner product $\langle \cdot, \cdot \rangle_{L^2(\Gamma_r)}$ is given by

$$\langle u^s(x_r, d_y), G(x_r, x) \rangle_{L^2(\Gamma_r)} := \int_{\Gamma_r} u^s(x_r, d_y) \overline{G(x_r, x)} ds$$

and

$$\begin{aligned} \|u^s(\cdot, d_y)\|_{L^2(\Gamma_r)} &= \left(\int_{\Gamma_r} |u^s(x_r, d_y)|^2 d\sigma_{x_r} \right)^{\frac{1}{2}}, \\ \|G(\cdot, x)\|_{L^2(\Gamma_r)} &= \left(\int_{\Gamma_r} |G(x_r, x)|^2 d\sigma_{x_r} \right)^{\frac{1}{2}}. \end{aligned}$$

In order to fully utilize measurements from multiple measurement events, i.e., with incidences $d_{y,n} \in \mathbb{S}^M, n = 1, \dots, N$, we define an index function $I(x)$ to combine different values of $I(x, d_{y,n})$ in the following way:

$$I(x) = \max_{n=1,2,\dots,N} \{I(x, d_{y,n})\} \quad \forall x \in \Omega.$$

Here, I_m means the index function for the m th data set. It has been discussed theoretically and illustrated numerically in [33] that the function in (2.12) has a relatively large value when a sampling point x is close to an inhomogeneous inclusion in Ω and decays rapidly as x moves away from any of the inclusions.

We notice that in the two aforementioned examples, the choices of sampling points x places a crucial role in constructing the indicator functions (either $\eta(x)$ or $I(x)$ in the previous two examples), and appropriate choices of the mesh size (or the density of sampling points) are of importance for insuring the best possible quality of the reconstruction procedure.

3. Optimal mesh size with far-field data under plane wave illumination. In this section, we shall consider the optimal choice of the mesh size for the reconstruction of inclusions inside Ω from the far-field data. We consider the case when $\Gamma_r = R\mathbb{S}^{M-1}$, where $R \gg 1$. In this case, instead of having the scattered field u^s as measurement, we may assume that we have obtained our measurement as the far-field pattern u_∞ given by

$$(3.1) \quad u_\infty(d_x, d_y) = \lim_{|x| \rightarrow \infty} |x|^{\frac{M-1}{2}} \exp^{-ik|x|} u_s(|x|d_x, d_y),$$

where d_x and d_y belong to the unit sphere \mathbb{S}^{M-1} .

Hence, we assume that the measurements $u_\infty(d_x, d_y)$, where $d_x, d_y \in \mathbb{S}^{M-1}$, are performed. For small wave number k , the Born approximation shows that the far-field pattern can be expressed as

$$(3.2) \quad u_\infty(d_x, d_y) = \tilde{C}_{k,M} k^2 \int_{\Omega} q(z) e^{ik(d_x - d_y) \cdot z} dz + O(k^4 |C_{k,M}|^2),$$

where their error term is in L^2 , and

$$\tilde{C}_{k,M} = \frac{-i}{\sqrt{8\pi}} \left(\frac{k}{2\pi} \right)^{\frac{M-2}{2}} \exp \left(-\frac{(M-1)}{4} \pi i \right)$$

is a constant depending on the space dimension M and k . We have the following result from the Nyquist–Shannon sampling theorem.

THEOREM 3.1. *Let k be fixed and small. Denote by $\mathfrak{F}(q)(\xi)$ the Fourier transform of $q(y)$:*

$$(3.3) \quad \mathfrak{F}(q)(\xi) := \int_{\Omega} q(z) e^{i\xi \cdot z} dz \quad \text{for } \xi \in \mathbb{R}^M.$$

Suppose that $\mathfrak{F}(q)(\xi) = 0$ for all $|\xi| > 2k$. Then, the reconstruction of q from $u_\infty(d_x, d_y)$, where $d_x, d_y \in \mathbb{S}^{M-1}$, is with an error of order $O(k^2 |\tilde{C}_{k,M}|)$. The reconstruction can be performed with a choice of the mesh size $h < \frac{\lambda}{2}$, where $\lambda := 2\pi/k$ is the operating wavelength.

Proof. It is direct to observe that

$$(3.4) \quad \mathfrak{F}(q)(\xi) = \frac{1}{\tilde{C}_{k,M} k^2} u_\infty(d_x, d_y) + \mathcal{O}(k^2 |\tilde{C}_{k,M}|),$$

where $\xi := k(d_x - d_y) \in \{\xi : |\xi| \leq 2k\}$. Hence, from $u_\infty(d_x, d_y)$, $d_x, d_y \in \mathbb{S}^{M-1}$, we obtain the values of $\mathfrak{F}(q)(\xi)$ for $|\xi| \leq 2k$ up to an error of the order $\mathcal{O}(k^2 |\tilde{C}_{k,M}|)$ in L^2 . Since $\mathfrak{F}(q)(\xi) = 0$ for all $|\xi| > 2k$, we have $\mathfrak{F}(q)(\xi)$ up to an error of the order $\mathcal{O}(k^2 |\tilde{C}_{k,M}|)$ in L^2 . Applying the inverse Fourier transform, we obtain q up to an error of the order $\mathcal{O}(k^2 |\tilde{C}_{k,M}|)$ in L^2 . An application of the Nyquist–Shannon sampling theorem yields the last statement in the theorem with a choice of $h < \frac{\lambda}{2}$. \square

Notice that the above result shows that we may maximize our choice of the mesh size by taking $h = \frac{\lambda}{2} - \epsilon$ for a small ϵ in order to minimize the computation complexity.

In order to recover the contrast function $q(x)$, we should discretize (3.2) into the following form:

$$u_\infty \approx \gamma k^2 \sum_{j=1}^N s_j q(z_j) e^{ik(d_x - d_y) \cdot z_j}.$$

Here, the optimal N is $\lceil 4|\Omega|/\lambda^2 \rceil$ when $M = 2$, where $\lceil x \rceil$ means the largest integer that is less than or equal to x , s_j denotes the j th grid point in Ω , and $|\Omega|$ represents the area (volume) of Ω .

4. Optimal mesh size with near-field data under point source illumination. In this section, optimal mesh size for contrast reconstruction from near-field data will be discussed. Based on the first term of the Neumann series solution to the Lippmann–Schwinger integral equation, which is known as the Born approximation, the scattered field u^s is approximated by

$$(4.1) \quad u_B^s(x, y) = k^2 \int_{\Omega} q(z) G(x, z) u^i(y, z) dz + O(k^4), \quad x \in \Gamma_r \text{ and } y \in \Gamma_s.$$

Furthermore, the incident field u^i in this case is provided by the Green function. Thus, the estimated scattered field u_B^s can be written into the following multistatic response (MSR):

$$(4.2) \quad \begin{aligned} [\text{MSR}(q)](x, y) &:= \frac{1}{k^2} u_B^s(x, y) \\ &= \int_{\Omega} q(z) G(x, z) G(z, y) dz + O(k^2), \quad x \in \Gamma_r \text{ and } y \in \Gamma_s. \end{aligned}$$

In practice, we again discretize the sampling domain D into N subregions and denote the center of each subregion by z_j for $j = 1, 2, \dots, N$. Based on this discretization, we have the following MSR approximation operator A up to a normalization constant $\tilde{C}_{k,M}$ depending on k and M , which is the dominant part of the near-field data,

$$(4.3) \quad A := \sum_{j=1}^N q(z_j) |z_j - x|^{\frac{2-M}{2}} |z_j - y|^{\frac{2-M}{2}} H_{\frac{M-2}{2}}^{(1)}(k|z_j - x|) H_{\frac{M-2}{2}}^{(1)}(k|z_j - y|) \\ \text{for } x \in \Gamma_r \text{ and } y \in \Gamma_s,$$

where $z_j \in \Omega$.

Let us consider for simplicity the case when $\Gamma_r = \Gamma_s$. In order to investigate the optimal mesh size for the reconstruction process, we need to determine the number of observable singular values for the MSR operator A when z_j are close to each other.

For this purpose, we first define a conjugation map on $L^2(\Gamma)$ as follows:

$$C : L^2(\Gamma) \rightarrow L^2(\Gamma) \quad f \mapsto \bar{f}.$$

Now, from the fact that the operator A is compact and C -complex symmetric, namely, $A^* = CAC$, we have the following Danciger's variational principle for the singular values $\{\sigma_i\}$ of A [21],

$$(4.4) \quad \sigma_n = \min_{\text{codim}_{\mathbb{R}} V = n} \max_{\substack{p \in V \\ \|p\|=1}} \Re[Ap, p],$$

where $[Ap, p] = p^T Ap$ and $\sigma_0 \geq \sigma_1 \geq \dots \geq 0$.

Before we state the following main result, we denote the locations of receivers and sources by $\Gamma := \Gamma_r \cup \Gamma_s$. First, we consider the simplest case when $N = 1$. Because $q(z_1)$ is a scalar, we investigate the following operator A_1 , which is the key part of the operator A :

$$(4.5) \quad \begin{aligned} A_1 &:= a|z - x|^{\frac{2-M}{2}}|z - y|^{\frac{2-M}{2}} H_{\frac{M-2}{2}}^{(0)}(k|z - x|) H_{\frac{M-2}{2}}^{(1)}(k|z - y|) \\ &= \varpi \otimes \varpi^T \quad \text{for } x, y \in \Gamma, \end{aligned}$$

where $a = \||z - x|^{\frac{2-M}{2}} H_{\frac{M-2}{2}}^{(1)}(k|z - x|)\|_{L^2(\Gamma)}^2$, \otimes means the Kronecker product, and

$$\varpi := |z - x|^{\frac{2-M}{2}} H_{\frac{M-2}{2}}^{(1)}(k|z - x|) / \left\| |z - x|^{\frac{2-M}{2}} H_{\frac{M-2}{2}}^{(1)}(k|z - x|) \right\|_{L^2(\Gamma)}$$

is a unit vector. It is easy to see that

$$(4.6) \quad \Re[A_1 p, p] = \Re(p^T A_1 p) = \Re(\varpi^T p)^2 \begin{cases} = 0 & \text{if } p \perp_{\mathbb{R}} \overline{\varpi}, \\ \neq 0 & \text{otherwise,} \end{cases}$$

and that $\Re[A_1 p, p] \leq 1$. We infer from Danciger's principle [18] that the singular values of A_1 are as follows: $\sigma_0 = 1$ and $\sigma_i = 0$ ($i \geq 1$).

Second, we investigate the case when $N = 2$. With the help of (4.3), the main part of the MSR matrix is of the form

$$(4.7) \quad A_2 := b_1 \varpi_1 \otimes \varpi_1^T + b_2 \varpi_2 \otimes \varpi_2^T,$$

where $b_j = \||z_j - x|^{\frac{2-M}{2}} H_{\frac{M-2}{2}}^{(1)}(k|z_j - x|)\|_{L^2(\Gamma)}^2$ and

$$\varpi_j := |z_j - x|^{\frac{2-M}{2}} H_{\frac{M-2}{2}}^{(1)}(k|z_j - x|) / \left\| |z_j - x|^{\frac{2-M}{2}} H_{\frac{M-2}{2}}^{(1)}(k|z_j - x|) \right\|_{L^2(\Gamma)}$$

for $j = 1, 2$ are unit vectors. Similarly, we are able to directly obtain that

$$(4.8) \quad \Re[A_2 p, p] = \Re(p^T A_2 p) \begin{cases} = 0 & \text{if } p \perp_{\mathbb{R}} \text{span}_{\mathbb{R}}\{\overline{\varpi}_1, \overline{\varpi}_2\}, \\ \neq 0 & \text{otherwise.} \end{cases}$$

Now, let us define $\{\overline{h_1}, \overline{h_2}\} := \{\frac{\overline{\varpi_1 + \varpi_2}}{\|\varpi_1 + \varpi_2\|_{L^2(\Gamma)}}, \frac{\overline{\varpi_1 - \varpi_2}}{\|\varpi_1 - \varpi_2\|_{L^2(\Gamma)}}\}$. Then, we have

$$(4.9) \quad \|h_1\|_{L^2(\Gamma)} = \|h_2\|_{L^2(\Gamma)} = 1, \quad \Re\langle h_1, h_2 \rangle_\Gamma = 0,$$

and that $\text{span}_{\mathbb{R}}\{\overline{h_1}, \overline{h_2}\} = \text{span}_{\mathbb{R}}\{\overline{\varpi_1}, \overline{\varpi_2}\}$. Hence, the operator A_2 can be written as

$$(4.10) \quad A_2 = \frac{1}{2} \|\varpi_1 + \varpi_2\|_{L^2(\Gamma)}^2 h_1 \otimes h_1^T + \frac{1}{2} \|\varpi_1 - \varpi_2\|_{L^2(\Gamma)}^2 h_2 \otimes h_2^T.$$

Considering (4.8)–(4.10), Danciger's principle yields that the singular values of A_2 satisfy

$$(4.11) \quad \sigma_0 = \frac{1}{2} \max \left\{ \|\varpi_1 + \varpi_2\|_{L^2(\Gamma)}^2, \|\varpi_1 - \varpi_2\|_{L^2(\Gamma)}^2 \right\} = 1 + |\Re\langle \varpi_1, \varpi_2 \rangle|,$$

$$(4.12) \quad \sigma_1 = \frac{1}{2} \min \left\{ \|\varpi_1 + \varpi_2\|_{L^2(\Gamma)}^2, \|\varpi_1 - \varpi_2\|_{L^2(\Gamma)}^2 \right\} = 1 - |\Re\langle \varpi_1, \varpi_2 \rangle|,$$

$$(4.13) \quad \sigma_l = 0 \quad \forall l > 1,$$

where $\langle \varpi_1, \varpi_2 \rangle = \int_{\Gamma} \overline{\varpi_1} \varpi_2 d\sigma$. The above results can be summarized in the following theorem.

THEOREM 4.1. *Suppose that the operator A can be represented as follows,*

$$(4.14) \quad A := w_1 \otimes w_1^T + w_2 \otimes w_2^T,$$

where w_j are unit vectors in $L^2(\Gamma)$ for $j = 1, 2$. We have the following expression for the singular values of A :

$$(4.15) \quad \sigma_0 = 1 + |\Re\langle w_1, w_2 \rangle|, \quad \sigma_1 = 1 - |\Re\langle w_1, w_2 \rangle|, \quad \sigma_2 = \sigma_3 = \dots = 0,$$

and the quotient α between the two nonzero singular values is expressed as

$$(4.16) \quad \alpha := \frac{\sigma_1}{\sigma_0} = \frac{1 - |\Re\langle w_1, w_2 \rangle|}{1 + |\Re\langle w_1, w_2 \rangle|}.$$

We have noticed that the ratio α represents the relative observability of the second singular value with respect to the first one. Therefore, it quantifies the ability to distinguish between two inhomogeneities from the measurements in the form of the MSR matrix. Consequently, we introduce the following definition of the α -distinguishable with respect to Γ for $0 < \alpha < 1$.

DEFINITION 4.2. *Two point scatterers at locations z_1 and z_2 with equal weights are α -distinguishable with respect to Γ_r if the following inequality is satisfied:*

$$(4.17) \quad 1 - \alpha \geq \frac{1 - |\Re\langle w_1, w_2 \rangle|}{1 + |\Re\langle w_1, w_2 \rangle|},$$

where

$$w_j := (k|z_j - x|)^{\frac{2-M}{2}} H_{\frac{M-2}{2}}^{(1)}(k|z_j - x|) / \left\| (k|z_j - x|)^{\frac{2-M}{2}} H_{\frac{M-2}{2}}^{(1)}(k|z_j - x|) \right\|_{L^2(\Gamma)}$$

with $j = 1, 2$ and $\forall z_j \in D, x \in \Gamma_r$.

Before proceeding further, let us provide an intuition behind our definition of α -distinguishability as a measure of resolution and how that definition is related to noise. Assuming that we have noisy measurement data and that we numerically observe that the second largest eigenvalue is close to zero, we may not be able to judge whether there is only one inclusion and the nonzero eigenvalue actually comes from noise, or that it comes from two inclusions that are very close to each other. The threshold of α -distinguishability is essentially measuring this in the following sense: given an α , there is a certain distance $d_{\alpha,z}$ depending on α and the sampling point z such that we shall not consider the second eigenvalue as a result of noise if our choice of mesh has a mesh-size $h_z < d_{\alpha,z}$ in a neighborhood of the sampling point z .

Without loss of generality, we consider two point scatterers located at $z_1 = z$ and $z_2 = z + \varepsilon v$, where v is a unit vector and ε is a distance parameter which can be viewed as the mesh size. We acquire the interval of ε when the two point scatterers are α -distinguishable with respect to Γ . From the series expansion of $(1+a)^{-\beta}$ for all $\beta \neq 0$ w.r.t. a , we derive that if $\varepsilon < |z-x|$, then

$$|z + \varepsilon v - x|^{-\beta} = \sum_{r=0}^{\infty} \sum_{s=0}^r \frac{\Gamma(\frac{\beta}{2} + r)}{\Gamma(\frac{\beta}{2}) s! (r-s)!} (-1)^r \varepsilon^{r+s} \cos^{r-s}(\theta_{z-x,v}) |z - x|^{-\beta-r-s},$$

where $\theta_{z-x,v}$ denotes the relative angle between $z - x$ and v and that the series converges absolutely and uniformly when $\varepsilon < (1-\gamma) \min\{1, |z-x|\}$ for some $0 < \gamma < 1$. Together with Graf's formula [34], we have if $\varepsilon < (1-\gamma) \min\{1, \text{dist}(\Gamma, z)\}$, then the following expansion holds:

$$(4.18) \quad \begin{aligned} & \Re \left(\int_{\Gamma} |z - x|^{\frac{2-M}{2}} |z + \varepsilon v - x|^{\frac{2-M}{2}} H_{\frac{M-2}{2}}^{(2)}(k|z-x|) H_{\frac{M-2}{2}}^{(1)}(k|z+\varepsilon v-x|) d\sigma_x \right) \\ &= \begin{cases} \sum_{n \in \mathbb{Z}} p_n J_n(k\varepsilon) & \text{if } M = 2, \\ \sum_{n \in \mathbb{Z}} \sum_{r \in \mathbb{N}} \sum_{s=0}^r p_{nrs} J_n(k\varepsilon) \varepsilon^{r+s} & \text{if } M > 2, \end{cases} \end{aligned}$$

where p_n and $p_{n,r,s}$ are explicitly given by

$$(4.19) \quad p_n := \Re \left(\int_{\Gamma} H_0^{(2)}(k|z-x|) H_n^{(1)}(k|z-x|) e^{-in\theta_{z-x,v}} d\sigma_x \right)$$

$$(4.20) \quad \begin{aligned} p_{nrs} := & (-1)^r \frac{\Gamma(\frac{M-2}{4} + r)}{\Gamma(\frac{M-2}{4}) s! (r-s)!} \\ & \Re \left(\int_{\Gamma} |z - x|^{2-M-r-s} H_{\frac{M-2}{2}}^{(2)}(k|z-x|) \right. \\ & \quad \cdot H_{\frac{M-2}{2}+n}^{(1)}(k|z-x|) \cos^{r-s}(\theta_{z-x,v}) e^{-in\theta_{z-x,v}} d\sigma_x \left. \right) \end{aligned}$$

with $\theta_{z-x,v}$ denoting the relative angle between $z - x$ and v . Likewise, we have

$$(4.21) \quad \begin{aligned} & \int_{\Gamma} |z + \varepsilon v - x|^{2-M} H_{\frac{M-2}{2}}^{(2)}(k|z+\varepsilon v-x|) H_{\frac{M-2}{2}}^{(1)}(k|z+\varepsilon v-x|) d\sigma_x \\ &= \begin{cases} \sum_{n,m \in \mathbb{Z}} h_{nm} J_n(k\varepsilon) J_m(k\varepsilon) & \text{if } M = 2, \\ \sum_{n,m \in \mathbb{Z}} \sum_{r \in \mathbb{N}} \sum_{s=0}^r h_{nmrs} J_n(k\varepsilon) J_m(k\varepsilon) \varepsilon^{r+s} & \text{if } M > 2, \end{cases} \end{aligned}$$

where h_{nm} and h_{nmrs} are given by

$$(4.22) \quad h_{nm} := \Re \left(\int_{\Gamma} H_m^{(2)}(k|z-x|) H_n^{(1)}(k|z-x|) e^{-i(n-m)\theta_{z-x,v}} d\sigma_x \right),$$

$$\begin{aligned} h_{nmrs} &:= (-1)^r \frac{\Gamma(\frac{M-2}{2} + r)}{\Gamma(\frac{M-2}{2}) s! (r-s)!} \\ &\cdot \Re \left(\int_{\Gamma} |z-x|^{2-M-r-s} H_{\frac{M-2}{2}+m}^{(2)}(k|z-x|) \right. \\ (4.23) \quad &\left. \cdot H_{\frac{M-2}{2}+n}^{(1)}(k|z-x|) \cos^{r-s}(\theta_{z-x,v}) e^{-i(n-m)\theta_{z-x,v}} d\sigma_x \right). \end{aligned}$$

Assume that $0 < R_0 \leq \text{dist}(z, \Gamma) \leq R_1$ for some $R_0, R_1 \in \mathbb{R}$, and consider the asymptotic property of J_m [9]. We can infer that both the series (4.18) and (4.21) converge absolutely. If we further impose the restriction that $\frac{k\varepsilon}{2} \leq 1$, then from the following well-known Taylor series of the Bessel functions [34],

$$(4.24) \quad J_n(k\varepsilon) = (\text{sgn}(n))^n \sum_{l \in \mathbb{N}} \frac{(-1)^l}{l!(l+|n|)!} \left(\frac{k\varepsilon}{2} \right)^{2l+|n|},$$

we immediately obtain the following expansion of the inner product:

$$\begin{aligned} &\Re \left(\int_{\Gamma} |z-x|^{\frac{2-M}{2}} |z+\varepsilon v - x|^{\frac{2-M}{2}} H_{\frac{M-2}{2}}^{(2)}(k|z-x|) H_{\frac{M-2}{2}}^{(1)}(k|z+\varepsilon v - x|) d\sigma_x \right) \\ (4.25) \quad &= \begin{cases} \sum_{l \in \mathbb{N}} \sum_{n \in \mathbb{Z}} (\text{sgn}(n))^n p_n \frac{(-1)^l}{l!(l+|n|)!} \left(\frac{k\varepsilon}{2} \right)^{2l+|n|} & \text{for } M = 2, \\ \sum_{l \in \mathbb{N}} \sum_{n \in \mathbb{Z}} \sum_{r \in \mathbb{N}} \sum_{s=0}^r (-\text{sgn}(n))^n p_{nrs} \frac{(-1)^l}{l!(l+|n|)!} \left(\frac{k\varepsilon}{2} \right)^{2l+|n|} \varepsilon^{r+s} & \text{for } M > 2, \end{cases} \end{aligned}$$

$$\begin{aligned} &\int_{\Gamma} |z+\varepsilon v - x|^{2-M} H_{\frac{M-2}{2}}^{(2)}(k|z+\varepsilon v - x|) H_{\frac{M-2}{2}}^{(1)}(k|z+\varepsilon v - x|) d\sigma_x \\ (4.26) \quad &= \begin{cases} \sum_{l,p \in \mathbb{N}} \sum_{n,m \in \mathbb{Z}} (\text{sgn}(n))^n (\text{sgn}(m))^m h_{nm} \frac{(-1)^{l+p}}{l!p!(l+|n|)!(p+|m|)!} \\ \left(\frac{k\varepsilon}{2} \right)^{2(l+p)+|n|+|m|} & \text{for } M = 2, \\ \sum_{l,p \in \mathbb{N}} \sum_{n,m \in \mathbb{Z}} \sum_{r \in \mathbb{N}} \sum_{s=0}^r (\text{sgn}(n))^n (\text{sgn}(m))^m h_{nmrs} \frac{(-1)^{l+p}}{l!p!(l+|n|)!(p+|m|)!} \\ \left(\frac{k\varepsilon}{2} \right)^{2(l+p)+|n|+|m|} \varepsilon^{r+s} & \text{for } M > 2, \end{cases} \end{aligned}$$

where the two series at the right-hand side converge absolutely for $\frac{k\varepsilon}{2} \leq 1$ and $\varepsilon < (1-\gamma) \min\{1, \text{dist}(\Gamma, z)\}$.

4.1. α -distinguishability when $M = 2$. For simplicity, let us first focus on the case when $M = 2$. We obtain the following estimate

$$(4.27) \quad \left| \Re \left(\int_{\Gamma} H_0^{(2)}(k|z-x|) H_0^{(1)}(k|z+\varepsilon v-x|) d\sigma_x \right) - p_0 + \frac{k\varepsilon}{2}(p_1 - p_{-1}) \right| \leq C_1 \frac{k^2 \varepsilon^2}{4},$$

$$(4.28) \quad \left| \int_{\Gamma} H_0^{(2)}(k|z+\varepsilon v-x|) H_0^{(1)}(k|z+\varepsilon v-x|) d\sigma_x - h_{00} - \frac{k\varepsilon}{2} \sum_{|m|+|n|=1} (\text{sgn}(n))^n (\text{sgn}(m))^m h_{nm} \right| \leq C_2 \frac{k^2 \varepsilon^2}{4},$$

where $p_0 = h_{00} = \|H_0^{(1)}(k|z-x|)\|_{L^2(\Gamma)}^2$ and C_1 and C_2 are two finite constants having the following forms:

$$(4.29) \quad C_1 = \sum_{l>0} \sum_{n \in \mathbb{Z}} \frac{|p_n|}{l!(l+n)!} + \sum_{n>1} \frac{|p_n|}{n!},$$

$$(4.30) \quad C_2 = \sum_{l+p>0} \sum_{m,n \in \mathbb{Z}} \frac{|h_{nm}|}{l!p!(l+n)!(p+m)!} + \sum_{m+n>1} \frac{|h_{nm}|}{n!m!}$$

if $\frac{k\varepsilon}{2} \leq 1$ and $\varepsilon < (1-\gamma) \min\{1, \text{dist}(\Gamma, z)\}$. From (4.27) and (4.28), we have the following approximation:

$$(4.31) \quad 1 - |\Re \langle w_1, w_2 \rangle|^2 = 1 - \frac{\left(p_0 - (p_1 - p_{-1}) \frac{k\varepsilon}{2} + \mathcal{O}\left(\frac{k^2 \varepsilon^2}{4}\right) \right)^2}{p_0 \left(p_0 + \frac{k\varepsilon}{2} \sum_{|m|+|n|=1} (\text{sgn}(n))^n (\text{sgn}(m))^m h_{nm} + \mathcal{O}\left(\frac{k^2 \varepsilon^2}{4}\right) \right)}.$$

We further assume that

$$(4.32) \quad \frac{k\varepsilon}{2} \leq \sqrt{\frac{p_0^2 k_1^2}{4C_2^2} + \frac{p_0(1-\delta)}{C_2}} - \frac{p_0 |k_1|}{2C_2}$$

for some $0 < \delta < 1$, where

$$(4.33) \quad k_1 = \frac{\sum_{|m|+|n|=1} (\text{sgn}(n))^n (\text{sgn}(m))^m h_{nm}}{p_0}.$$

Then, we have

$$(4.34) \quad \max \left\{ \frac{k\varepsilon}{2} \left| k_1 - \frac{C_2 k\varepsilon}{p_0} \right|, \frac{k\varepsilon}{2} \left| k_1 + \frac{C_2 k\varepsilon}{p_0} \right| \right\} \leq 1 - \delta,$$

and thus we can derive from the Taylor expansion and (4.31) that

$$(4.35) \quad \left| 1 - |\Re\langle w_1, w_2 \rangle|^2 - \left(\frac{2(p_1 - p_{-1})}{p_0} + k_1 \right) \frac{k \varepsilon}{2} \right| \leq C \frac{k^2 \varepsilon^2}{4}$$

with the constant C given by

$$(4.36) \quad \begin{aligned} C = & \frac{C_2}{p_0} (1 + 2|k_1| \delta^{-1}) + k_1^2 \delta^{-1} + \frac{C_2^2}{p_0^2} \delta^{-1} \\ & + \frac{2(|p_1| + |p_{-1}|)|k_1|}{p_0} + \frac{(|p_1| + |p_{-1}|)^2 + 2(p_0 + |p_1| + |p_{-1}|)C_1 + C_1^2}{p_0^2} \end{aligned}$$

when $0 < \delta < 1$. We can rewrite the condition in (4.17) as follows:

$$(4.37) \quad \frac{4(1-\alpha)}{(2-\alpha)^2} \geq 1 - |\Re\langle w_1, w_2 \rangle|^2.$$

With the help of (4.35), the two point inclusions with the same magnitude are α -distinguishable if the following inequality holds:

$$(4.38) \quad \frac{4(1-\alpha)}{(2+\alpha)^2} \geq \left(\frac{2(p_1 - p_{-1})}{p_0} + k_1 \right) \frac{k \varepsilon}{2} + C \left(\frac{k \varepsilon}{2} \right)^2.$$

This directly implies the following theorem. Note that we may always assume that $k \varepsilon < 1/2$.

THEOREM 4.3. *When the dimension $M = 2$, consider a point z such that $0 < R_0 \leq \text{dist}(z, \Gamma) \leq R_1$ for some $R_0, R_1 \in \mathbb{R}$, where $\Gamma = \Gamma_s = \Gamma_r$, $\frac{k \varepsilon}{2} \leq \min\{\frac{1}{4}, \sqrt{\frac{p_0^2 k_1^2}{4C_2^2} + \frac{p_0(1-\delta)}{C_2} - \frac{p_0|k_1|}{2C_2}}\}$ for some $0 < \delta < 1$, $\varepsilon < (1-\gamma) \min\{1, \text{dist}(\Gamma, z)\}$ for some $0 < \gamma < 1$, p_n are defined as in (4.19), and h_{nm} as in (4.22), and let C_1, C_2, C, k_1 be as stated in (4.29), (4.30) (4.36), and (4.33), respectively. The two point scatterers with equal weights located at z and $z + \varepsilon v$ are α -distinguishable with respect to Γ if the following inequality holds:*

$$(4.39) \quad \frac{k \varepsilon}{2} \leq - \left(\frac{2p_1 - 2p_{-1} + k_1 p_0}{2C p_0} \right) + \sqrt{\left(\frac{2p_1 - 2p_{-1} + k_1 p_0}{2C p_0} \right)^2 + \frac{16(1-\alpha)}{C(2+\alpha)^2}}.$$

Unfortunately, both the conditions and conclusions of the above theorem are too complicated to be practical for choosing an optimal mesh size. In order to obtain an optimal mesh size for practical use, we provide approximations for the coefficients in the above inequalities: we estimate C_1 and C_2 by

$$(4.40) \quad C_1 \approx p_0, \quad C_2 \approx 2p_0.$$

By considering (4.25) and (4.26), and further imposing that $\delta = 1/2$, the following approximation of the constant C holds:

$$(4.41) \quad C \approx 13 + 8|k_1| + 2k_1^2 + \frac{(|p_1| + |p_{-1}|)^2 + 2(|p_1| + |p_{-1}|)(1 + |k_1|)p_0}{p_0^2}.$$

The condition (4.32) with $k\varepsilon/2 < 1/4$ can also be simplified to be the above approximate condition

$$(4.42) \quad \frac{k\varepsilon}{2} < \min \left\{ \frac{1}{4}, \sqrt{\frac{k_1^2}{16} + \frac{1}{4}} - \frac{|k_1|}{4} \right\}.$$

Combining the above estimations of the constants C_1, C_2 , and C with (4.39), we obtain the following approximate description of an *anisotropic* optimal density at any point z and any direction v for contrast reconstruction from the near-field data in terms of the α -distinguishably,

$$(4.43) \quad h_{z,v}(\alpha) := \frac{2}{k} \min \left\{ \frac{1}{4}, \sqrt{\frac{k_1^2}{16} + \frac{1}{4}} - \frac{|k_1|}{4}, \left(\frac{2p_1 - 2p_{-1} + k_1 p_0}{2Cp_0} \right) - \sqrt{\left(\frac{2p_1 - 2p_{-1} + k_1 p_0}{2Cp_0} \right)^2 + \frac{16(1-\alpha)}{C(2+\alpha)^2}} \right\}.$$

Note that p_0, p_1, p_{-1}, k_1 , and C depend on z, v , and Γ .

Remark 4.4. A few remarks are in order:

- (i) In practice, the measurements are taken over a finite number of points on $\Gamma = \Gamma_r = \Gamma_s$, and hence the integrals in (4.19), (4.20), (4.22), and (4.23) can be evaluated numerically as a sum over the points.
- (ii) In practice, small regions with fine details are usually anticipated to be recovered with high resolution. Thus, a uniform discretization in the whole sampling domain may not be the best. Hence, we may apply adaptivity and use the optimal mesh size in (4.43) in the region with the requirements of high resolution and a coarse mesh to the other regions.
- (iii) To get the interpretation of the optimal mesh size correct, actually it means if you refine further than the mesh size given, it will not improve the resolution. Hence, if the object is far away, then it is almost identical to using far-field reconstruction, and we do not need to refine better than $\lambda/2$.
- (iv) A similar analysis can be performed in the general case when Γ_r and Γ_s may not coincide, but we skip the analysis for the sake of simplicity.
- (v) A similar analysis may be performed with a number of inclusions $N > 2$ or with more complicated situations, e.g., with contrasts of different magnitudes, or with different sizes for the inclusions. Nonetheless, we notice that in a more complicated setting, the criterion of an optimal mesh-size hence obtained would be more complicated to be verified and computed numerically. Meanwhile, the imaging quality of using a more complicated description rule of an optimal mesh-size would not necessarily improve. Especially when the analysis in this section is providing us a bottom line in the sense that if we further refine, we shall not expect improvement even in a simple case, and we shall not expect improvement in a more complicated case. Considering the balance between the computational complexity of the description rule of the optimal mesh-size we would obtain and the slim possible improvement when a more complicated rule is employed, we decide that our analysis presented in this work shall focus only on the case when $N = 2$ with equal contrast for the sake of clarity of the exposition. We shall postpone the analysis of more complicated cases to future discussions.

4.2. α -distinguishability when $M > 2$. Similarly, when $M > 2$, we have

$$(4.44) \quad \left| \Re \left(\int_{\Gamma} H_0^{(2)}(k|z-x|) H_0^{(1)}(k|z+\varepsilon v-x|) d\sigma_x \right) - p_{000} + \frac{k\varepsilon}{2} \left(p_{100} - p_{-100} - \frac{2p_{010}}{k} \right) \right| \leq C_{1,M} \frac{k^2 \varepsilon^2}{4},$$

$$(4.45) \quad \left| \int_{\Gamma} H_0^{(2)}(k|z+\varepsilon v-x|) H_0^{(1)}(k|z+\varepsilon v-x|) d\sigma_x - h_{0000} + \frac{k\varepsilon}{2} \left(\sum_{|m|+|n|=1} (\operatorname{sgn}(n))^n (\operatorname{sgn}(m))^m h_{nm00} + \frac{2h_{0010}}{k} \right) \right| \leq C_{2,M} \frac{k^2 \varepsilon^2}{4},$$

where $p_{000} = h_{0000} = \| |z-x|^{\frac{M-2}{2}} H_{\frac{M-2}{2}}^{(1)}(k|z-x|) \|_{L^2(\Gamma)}^2$ and $C_{1,M}$ and $C_{2,M}$ are two constants given if $\frac{k\varepsilon}{2} \leq 1$ and $\varepsilon < (1-\gamma) \min\{1, \operatorname{dist}(\Gamma, z)\}$ by

$$(4.46) \quad C_{1,M} = \sum_{l>0} \sum_{n \in \mathbb{Z}} \sum_{r \in \mathbb{N}} \sum_{s=0}^r \frac{|p_{nrs}|}{l!(l+n)!} + \sum_{n>1} \sum_{r \in \mathbb{N}} \sum_{s=0}^r \frac{|p_{nrs}|}{n!},$$

$$(4.47) \quad C_{2,M} = \sum_{l+p>0} \sum_{m,n \in \mathbb{Z}} \sum_{r \in \mathbb{N}} \sum_{s=0}^r \frac{|h_{nmrs}|}{l!p!(l+n)!(p+m)!} + \sum_{m+n>1} \sum_{r \in \mathbb{N}} \sum_{s=0}^r \frac{|h_{nmrs}|}{n!m!}.$$

Hence, a similar analysis can be performed as in the previous subsection provided that $\varepsilon < (1-\gamma) \min\{1, \operatorname{dist}(\Gamma, z)\}$ and

$$(4.48) \quad \frac{k\varepsilon}{2} \leq \min \left\{ 1, \sqrt{\frac{p_{000}^2 k_1^2}{4C_{2,M}^2} + \frac{p_{000}(1-\delta)}{C_{2,M}}} - \frac{p_{000}|k_{1,M}|}{2C_{2,M}} \right\}$$

for some $0 < \delta < 1$, where

$$(4.49) \quad k_{1,M} = \left(\sum_{|m|+|n|=1} (\operatorname{sgn}(n))^n (\operatorname{sgn}(m))^m h_{nm00} + \frac{2h_{0010}}{k} \right) / p_{000}.$$

Then, by a Taylor expansion, we readily see that

$$\left| 1 - |\Re \langle w_1, w_2 \rangle|^2 - \left(\frac{2(p_{100} - p_{-100} - \frac{2p_{010}}{k})}{p_{000}} + k_{1,M} \right) \frac{k\varepsilon}{2} \right| \leq C \frac{k^2 \varepsilon^2}{4}$$

with the constant C_M being given by

$$(4.50) \quad \begin{aligned} C_M &= C_M \frac{C_{2,M}}{p_{000}} (1 + 2|k_{1,M}| \delta^{-1}) + k_{1,M}^2 \delta^{-1} \\ &+ \frac{C_{2,M}^2}{p_{000}^2} \delta^{-1} + \frac{2(|p_{100}| + |p_{-100}| - \frac{2|p_{010}|}{k}) |k_{1,M}|}{p_{000}} \\ &+ \frac{\left(|p_{100}| + |p_{-100}| - \frac{2|p_{010}|}{k} \right)^2 + 2 \left(p_{000} + \left(|p_{100}| + |p_{-100}| - \frac{2|p_{010}|}{k} \right) \right) C_{1,M} + C_{1,M}^2}{p_{000}^2} \end{aligned}$$

when $0 < \delta < 1$. Hence, condition (4.17) is fulfilled if

$$(4.51) \quad \frac{4(1-\alpha)}{(2+\alpha)^2} \geq \left(\frac{2(p_{100} - p_{-100} - \frac{2p_{010}}{k})}{p_{000}} + k_{1,M} \right) \frac{k\varepsilon}{2} + C_M \left(\frac{k\varepsilon}{2} \right)^2.$$

Likewise, adding the constraint $k\varepsilon < 1/4$, this directly infers the following theorem.

THEOREM 4.5. *For $M > 2$, consider a point z such that $0 < R_0 \leq \text{dist}(z, \Gamma) \leq R_1$ for some $R_0, R_1 \in \mathbb{R}$, where $\Gamma = \Gamma_s = \Gamma_r$, and that $\frac{k\varepsilon}{2}$ satisfies (4.48) for some $0 < \delta < 1$ and $k\varepsilon < 1/4$, $\varepsilon < (1-\gamma) \min\{1, \text{dist}(\Gamma, z)\}$ for some $0 < \gamma < 1$, where p_{nrs} are defined as in (4.20), h_{nmrs} as in (4.23), and let $C_{1,M}, C_{2,M}, C_M, k_{1,M}$ be as in (4.46), (4.47) (4.51), and (4.49), respectively. The two point scatterers with equal weights located at z and $z + \varepsilon v$ are α -distinguishable with respect to Γ if the following inequality holds:*

$$(4.52) \quad \frac{k\varepsilon}{2} \leq \left(\frac{2(p_{100} - p_{-100} - \frac{2p_{010}}{k})}{p_{000}} + k_{1,M} \right) - \sqrt{\left(\frac{2(p_{100} - p_{-100} - \frac{2p_{010}}{k})}{p_{000}} + k_{1,M} \right)^2 + \frac{16(1-\alpha)}{C_M(2+\alpha)^2}}.$$

In order to make the conditions stated in the above theorem practical, we assume that $\delta = 1/2$ and provide, by considering (4.25) and (4.26), approximations for the coefficients with

$$C_{1,M} \approx p_{000}, \quad C_{2,M} \approx 2p_{000},$$

$$C_M \approx 13 + 8|k_{1,M}| + 2k_{1,M}^2 + \frac{\left(|p_{100}| + |p_{-100}| - \frac{2|p_{010}|}{k}\right)^2 + 2\left(|p_{100}| + |p_{-100}| - \frac{2|p_{010}|}{k}\right)(p_{000} + |k_{1,M}|)}{p_{000}^2}.$$

With the above approximations of the constants $C_{1,M}, C_{2,M}$, and C_M and estimate (4.52), we obtain an *anisotropic* optimal density at any point z and at any direction v for contrast reconstruction from the near-field data in terms of α -distinguishability as follows:

$$(4.53) \quad h_{z,v,M}(\alpha) := \frac{2}{k} \min \left\{ \frac{1}{4}, \sqrt{\frac{k_{1,M}^2}{16} + \frac{1}{4} - \frac{|k_{1,M}|}{4}}, \left(\frac{2(p_{100} - p_{-100} - \frac{2p_{010}}{k})}{p_{000}} + k_{1,M} \right) - \sqrt{\left(\frac{2(p_{100} - p_{-100} - \frac{2p_{010}}{k})}{p_{000}} + k_{1,M} \right)^2 + \frac{16(1-\alpha)}{C_M(2+\alpha)^2}} \right\}.$$

The remarks in the previous subsection are also in order in this subsection.

4.2.1. Combining the optimal mesh size function along two opposite directions. Practically, one may combine the optimal mesh-size for v and $-v$ since they are refined in the same direction, and we may consider the following function instead,

$$\widetilde{h}_{z,v}(\alpha) := \min \{h_{z,v}(\alpha), h_{z,-v}(\alpha)\},$$

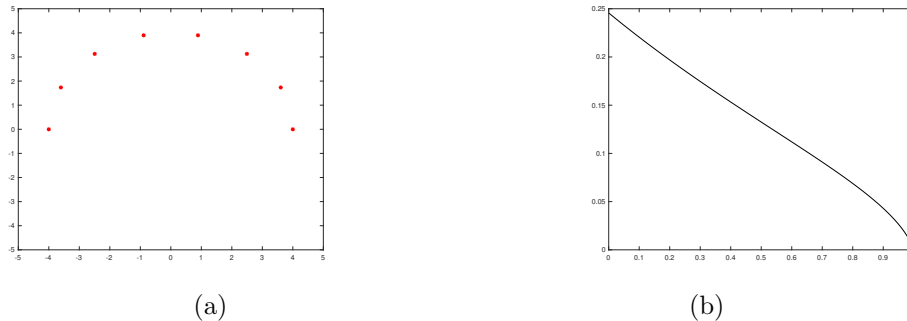


FIG. 3. (a) Γ in red. (b) The graph of $h_{z,v}(\alpha)$ with respect to α when $k = 2$, $z = (1, 3.5)$, and the polarization direction $v = (1, 0)$. Measurement points in red and grid points in blue.

as well as

$$\widetilde{h}_{z,v,M}(\alpha) := \min \{h_{z,v,M}(\alpha), h_{z,-v,M}(\alpha)\}.$$

This is to forget the information about separating a point forward or backward along the direction v .

5. Numerical illustrations. In this section, we shall exhibit some numerical simulations. First, we present the following adaptive refinement procedure, which can help to reduce the computational burden sharply in practice.

5.1. Adaptive refinement using the optimal mesh function. We can apply the function $\widetilde{h}_{z,v}(\alpha)$ to refine a mesh at a point z along a direction v (which we may refer to as a polarization direction). For a given point x in the sampling domain, let us denote $I(x)$ as the imaging function at the point x . Now, suppose we have a finite number of inhomogeneous inclusions inside Ω , and we implement the following procedures to recover all the inhomogeneities.

Algorithm I.

Given a threshold K_{thres} , select a coarse mesh with mesh size $h = \lambda/2$ and define S_0 as the mesh-points of this course mesh.

Then, for $k = 0, 1, \dots$, run the following:

- (i) Define the points $z \in S_k$ such that $I(z) > \max_{y \in S_k} I(y)$ as \bar{S}_k .
- (ii) For each $z \in \bar{S}_k$, locate one of the closest points $y_z \in \bar{S}_k$ such that $d(z, y_z) \leq \min_{x \in \bar{S}_k} d(z, x)$. Define the direction $v_z := (z - y_z)/|z - y_z|$.
- (iii) Refine the mesh $\widetilde{h}_{z,v_z}(\alpha)$ at the point z and the polarization direction v_z to obtain S_{k+1} such that $S_k \subset S_{k+1}$.
- (iv) Repeat the above until $S_k = S_{k+1}$.

5.2. Behavior of the mesh-size function $\widetilde{h}_{z,v}(\alpha)$. In order to understand better the behavior of the optimal mesh-size function, let us numerically illustrate some of the behaviors of $\widetilde{h}_{z,v}(\alpha)$ defined as in (4.43) (see Theorem 4.3). Assume that the sources x_s and receivers x_r are located at $\Gamma = \{(\cos(4\pi n/14), 4 \sin(2\pi n/14))\}$ for $n = 0, 1, \dots, 7$, as shown in Figure 3(a), and let $\Omega = B_4(0)$.

We assume that $k = 2$, $z = (1, 3.5)$, and the polarization direction $v = (1, 0)$. The mesh-size function $h_{z,v}(\alpha)$ with respect to α is illustrated in Figure 3(b). We may also fix a large α to obtain a density function and uneven mesh with a mesh-size

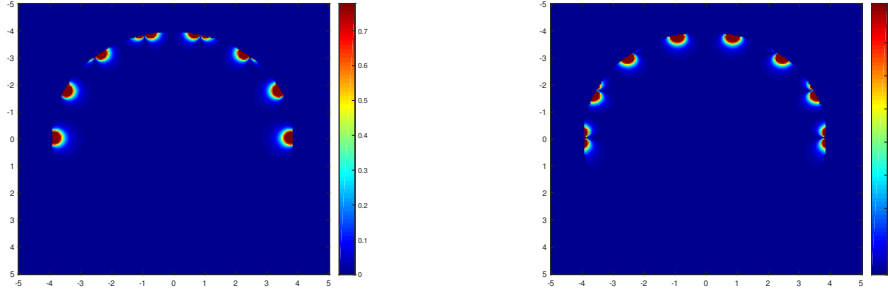


FIG. 4. The function $p_{v,\alpha}(z)$ at $v = (1,0)$ and $v = (0,1)$, respectively, when $\alpha = 0.99$. Measurement points in red and grid points in blue.

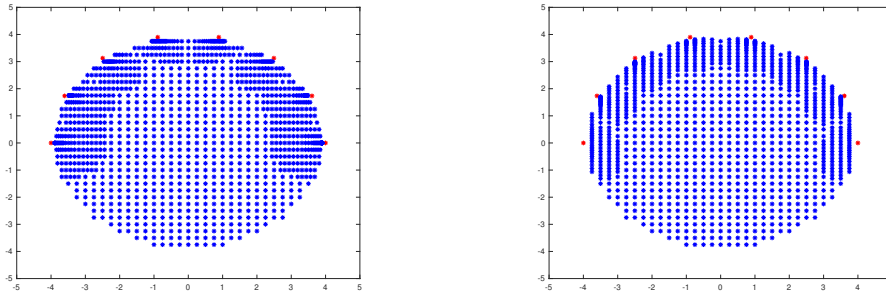


FIG. 5. Grid points with mesh-size satisfying $h_{z,v}(0.1)$ along the direction v , where $v = (1,0)$ and $v = (0,1)$, respectively.

satisfying the density provided by

$$z \mapsto p_{v,\alpha}(z) := \frac{(\widetilde{h}_{z,v}(\alpha))^{-2}}{\int_{\Omega} (\widetilde{h}_{z,v}(\alpha))^{-2} dz}$$

for a fixed v . The reason to take this function is that the optimal density is proportional to $(\widetilde{h}_{z,v}(\alpha))^{-M}$, where $M = 2$. Figure 4 shows the density function $p_{v,\alpha}(z)$ at $v = (1,0)$ and $v = (0,1)$, respectively, when $\alpha = 0.995$.

The above plots show that the refinement is unnecessary when the sampling points are at a distance half the radius from the sources/receivers. Now, we fix a particular α and generate a set of grid points with a mesh-size satisfying $h_{z,v}$ along the direction v . Figure 5 illustrates the grid points with $v = (1,0)$ and $v = (0,1)$, respectively, when $\alpha = 0.55$.

One may observe that the refinements are done in the directions v near the source/receiver points and are left coarser when the sampling points are further away. In practice, we may combine the two mesh sizes and generate a tensor mesh with a mesh-size $\widetilde{h}_{z,e_1}(\alpha)$ along $e_1 = (1,0)$ and $\widetilde{h}_{z,e_2}(\alpha)$ along $e_2 = (0,1)$. Figure 6, respectively, shows the grid points of the tensor mesh with $\widetilde{h}_{z,e_1}(\alpha)$ along $e_1 = (1,0)$ and $\widetilde{h}_{z,e_2}(\alpha)$ along $e_2 = (0,1)$ when $\alpha = 0.55$.

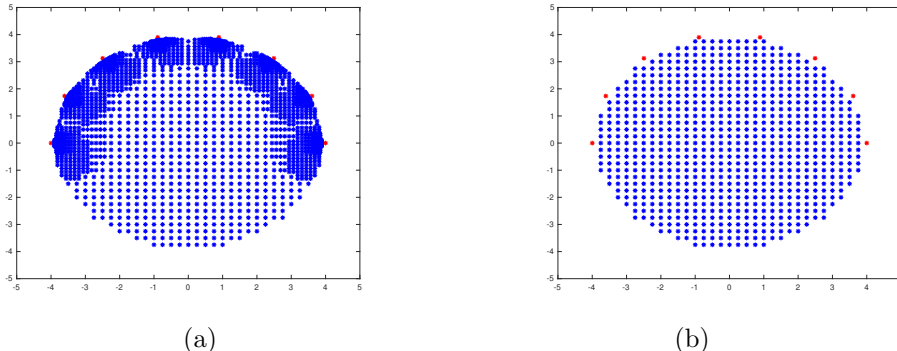


FIG. 6. (a) Grid points with mesh-size satisfying $\widetilde{h}_{z,v}(0.1)$ along the direction v , where $v = (1, 0)$ and $v = (0, 1)$, respectively. (b) Unrefined mesh. Measurement points in red and grid points in blue.

5.3. Use of the mesh-size function $\widetilde{h}_{z,v}(\alpha)$ for improving the reconstruction methods. This paper aims at getting an optimal mesh-size which maximizes the resolution of the reconstruction procedure with minimal numerical cost. As discussed before, this choice of mesh is not restricted to one particular numerical method, and the numerical methods given in subsection 2.2 are just several examples to illustrate the concept. In this subsection, we illustrate the efficiency of the optimal meshing procedure using the DSM, which is introduced in subsection 2.2. For further details on the DSM, we refer to [28, 29, 31, 14, 29, 32, 33, 15, 16, 25, 26, 27].

In what follows, we consider an example of a near-field measurement corresponding to only one illumination. Notice that since the case considered here is more pathological than the assumptions given in Theorem 4.3, the mesh-size function $\widetilde{h}_{z,v}(\alpha)$ defined as in (4.43) shall serve as a bottom line for the reconstruction.

We consider the case $k = \pi^2$ when $q(x)$ in (2.1) is given by

$$q(x) = 1 + 2\mathcal{I}_{Q_1}(x) + 2\mathcal{I}_{Q_2}(x),$$

where $Q_1 = \{x \in \mathbb{R}^2; -0.275 < x_1 < -0.175, -0.275 < x_2 < -0.175\}$ and $Q_2 = \{x \in \mathbb{R}^2; -0.15 < x_1 < -0.05, -0.15 < x_2 < -0.05\}$ are two squares inside \mathbb{R}^2 , and \mathcal{I}_A is an indicator function of a set A such that the value is 1 if $x \in A$ and is 0 otherwise. We take a plane wave incidence with angle $\theta_y = \pi/4$, i.e., $d_y = (\cos(\theta_y), \sin(\theta_y))$. As shown in the following figures, 20 measurement points along a circle of radius 0.5 are employed in this example.

We perform the DSM with different mesh sizes to illustrate the efficiency of using $\widetilde{h}_{z,v}(\alpha)$ for meshing. Note that we intentionally define Q_1 and Q_2 closer to the boundary measurement points; otherwise the density given by $\widetilde{h}_{z,v}(\alpha)$ will be similar to the situation when we have far-field measurements, and that will not serve the purpose of illustrating the efficiency of $\widetilde{h}_{x,v}(\alpha)$. Moreover, we also intentionally put the distance between Q_1 and Q_2 smaller than half of the wavelength, which is approximately 0.16. This helps to test if the meshing given by $\widetilde{h}_{x,v}(\alpha)$ can separate the two inclusions.

Before we continue to describe the result of our numerical experiments, we would like to clarify the purpose of our choice of numerical setup and design of our experiment. Our intention is to test the best performance possible of our optimal mesh size under a very ill-conditioning setting. With this understanding, we have intentionally chosen the DSM, which creates an image that is far from being perfect

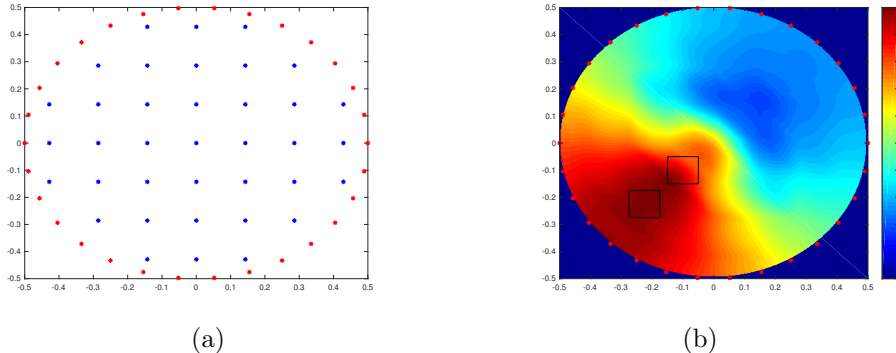


FIG. 7. (a) Grid points on a coarse mesh. (b) reconstruction given by $[I(x, dy)]^2$, where $I_{\text{coarse}} := I(x, dy)$ in (2.12) with the grid point given by the coarse mesh.

due to the minimality of data used to reconstruct the inclusions. As discussed in [14, 15, 16, 25, 26, 27, 28, 29, 31, 32, 33], it is clear that the image has a point spread function with a heavy tail, and hence the reconstruction shall not be expected to be sharp. Moreover, our reconstruction is based on one single incidence wave, which makes the problem more severely ill-posed. The purpose of the aforementioned choices are to test whether our optimal mesh-size will help improving the imaging even with this quite primitive and far-from-being-perfect setting. Our choice of the distance between scatterers serves a similar purpose: it is smaller than half of the wave-length and is known to be very challenging in numerical reconstruction. We therefore again expect that the reconstruction shall be far from perfect. Meanwhile, we hope to test whether our choice of optimal mesh-size helps improve the imaging even with this severely pathological setup.

Figure 7(a) illustrates the coarse mesh that we considered, with its mesh-size being half the wavelength. Figure 7(b) shows the reconstruction given by the index function $I_{\text{coarse}} := I(x, dy)$ with this coarse mesh. With this nonoptimal mesh-size, as we shall have expected, we cannot distinguish two inclusions in the image, and basically we only observe a large patch at the lower bottom part of the reconstruction and we are not able to separate the two inclusions.

Now, let us consider a refinement of the mesh as a tensor grid with mesh-sizes $\tilde{h}_{z,e_i}(\alpha)$ along the two directions $e_1 = (1, 0)$ and $e_2 = (0, 1)$, where we take $\alpha = 0.9$. We refine the mesh in the whole sampling domain Ω and obtain a fine mesh given as in Figure 8(a). We then perform the DMS and Figure 8(b) is the approximation provided by the index function $I(x, dy)$ with this fine sampling. We notice that this sampling helps to identify whether or not there are indeed two inclusions, with a clear dip separating the two inclusions. However, we do not expect a very fine reconstruction since the problem is severely ill-posed. Nonetheless, comparing to Figure 7(b), we can observe that with an optimal mesh-size, Figure 8(b) has an improved imaging quality and we are able to separate the two inclusions in the image even under this severely ill-conditioned setting.

Next, we consider an adaptive refinement of the mesh with refinement strategy chosen as Algorithm I with $K_{\text{thres}} = 0.995$. Again, we refine as a tensor grid with mesh-sizes $\tilde{h}_{z,e_i}(\alpha)$ along the two directions $e_1 = (1, 0)$ and $e_2 = (0, 1)$, where we take $\alpha = 0.9$. The resulting adaptive refinement is shown in Figure 9(a). We perform the DSM. Figure 9(b) illustrates the reconstructed image obtained by the index

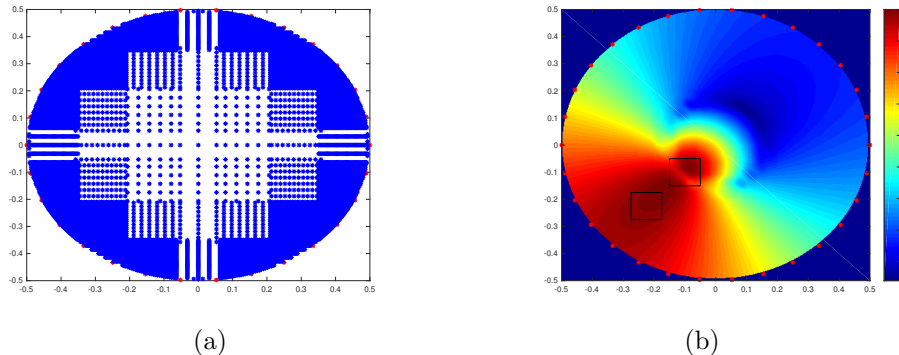


FIG. 8. (a) Grid points on a refined mesh given by a tensor grid with mesh-sizes $\widetilde{h_{x,e_i}}(\alpha)$ along $e_1 = (1,0), e_2 = (0,1)$, $\alpha = 0.9$, and x is taken in the whole sampling domain Ω . (b) A reconstruction given by $[I(x,dy)]^2$, where $I(x,dy)$ in (2.12) with a refined grid in the left.

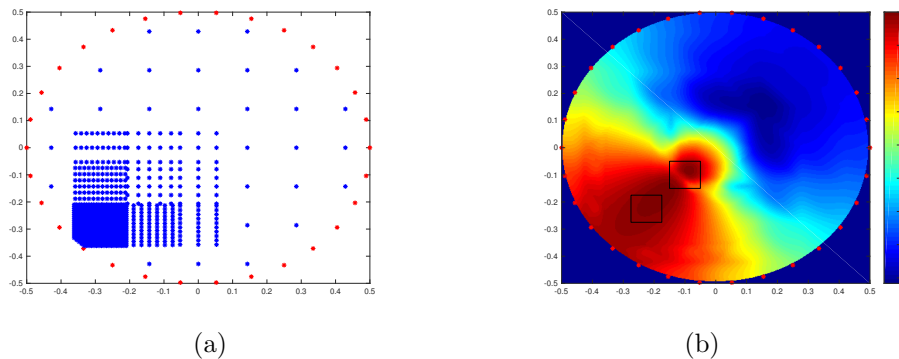


FIG. 9. (a) Grid points on adaptively refined mesh given by a tensor grid with mesh-sizes $\widetilde{h_{x,e_i}}(\alpha)$ along $e_1 = (1,0), e_2 = (0,1)$, $\alpha = 0.9$, with refinement strategy chosen as Algorithm I with $K_{\text{thres}} = 0.995$. (b) A reconstruction given by $[I(x,dy)]^2$, where $I(x,dy)$ in (2.12) with adaptively-refined grid on the left.

function $I(x,dy)$ with this adaptive fine sampling. Comparing the reconstructions in Figures 8 and 9, we observe a similar quality of the two reconstructions, i.e., both of them are able to separate the two inclusions. Meanwhile the image coming from adaptive refinement requires a significantly smaller number of sampling points in the reconstruction.

6. Conclusion. In this paper, we have discussed the choice of optimal mesh size for the reconstruction of inclusions from both the near-field and the far-field data in two and three dimensions. The computation complexity would be sharply reduced with an optimal mesh size for state-of-the-art algorithms (i.e., LSM, DSM, CSIM, etc.) since the computation complexity is usually at least of the order of $\mathcal{O}(N^{M-1})$ in \mathbb{R}^M , where N is the number of sampling points along one direction. Moreover, an optimized mesh size can help improving reconstructions of some iterative reconstruction approaches (i.e., MSM, EMSM, etc.) by avoiding choices of stopping criterion which may heavily depend on the quality of the reconstruction under a coarser mesh and a subjective choice of the cutoff value. We can conclude that our results are expected to have important implications in solving inverse scattering problems.

REFERENCES

- [1] H. AMMARI, Y.T. CHOW, AND J. ZOU, *Super-resolution in imaging high contrast targets from the perspective of scattering coefficients*, J. Math. Pures Appl. (9), 111 (2018), pp. 191–226.
- [2] H. AMMARI, J. GARNIER, W. JING, H. KANG, M. LIM, K. SØLNA, AND H. WANG, *Mathematical and Statistical Methods for Multistatic Imaging*, Lecture Notes in Math. 2098, Springer, Berlin, 2013.
- [3] H. AMMARI, J. GARNIER, V. JUGNON, AND H. KANG, *Stability and resolution analysis for a topological derivative based imaging functional*, SIAM J. Control Optim., 50 (2012), pp. 48–76.
- [4] H. AMMARI, J. GARNIER, H. KANG, L. NGUYEN, AND L. SEPPECHER, *Multi-Wave Medical Imaging*, Model. Simul. Med. Imaging 2, World Scientific, London, 2017.
- [5] H. AMMARI, E. IAKOVLEVA, AND H. KANG, *Reconstruction of a small inclusion in a 2D open waveguide*, SIAM J. Appl. Math., 65 (2005), pp. 2107–2127.
- [6] H. AMMARI, E. IAKOVLEVA, AND D. LESSELIER, *A MUSIC algorithm for locating small inclusions buried in a half-space from the scattering amplitude at a fixed frequency*, Multiscale Model. Simul., 3 (2005), pp. 597–628.
- [7] H. AMMARI, E. IAKOVLEVA, D. LESSELIER, AND G. PERRUSSON, *MUSIC-type electromagnetic imaging of a collection of small three-dimensional inclusions*, SIAM J. Sci. Comput., 29 (2007), pp. 674–709.
- [8] H. AMMARI AND H. ZHANG, *Super-resolution in high-contrast media*, Proc. A., 471 (2015), 20140946.
- [9] M. ABRAMOWITZ AND I. STEGUN, *Handbook of Mathematical Functions*, 9th ed., Dover, New York, 1970, pp. 365–366.
- [10] G. BAO, P. LI, AND H. WU, *An adaptive edge element method with perfectly matched absorbing layers for wave scattering by periodic structures*, Math. Comp., 79 (2010), pp. 1–34.
- [11] G. BAO AND L. ZHANG, *Shape reconstruction of the multi-scale rough surface from multi-frequency phaseless data*, Inverse Problems, 32 (2016), 085002.
- [12] P. VAN DEN BERG, A. BROEKHOVEN, AND A. ABUBAKAR, *Extended contrast source inversion*, Inverse Problems, 15 (1999), pp. 1325–1344.
- [13] M. CHENEY, *The linear sampling method and the MUSIC algorithm*, Inverse Problems, 17 (2001), pp. 591–595.
- [14] Y.T. CHOW, K. ITO, K. LIU, AND J. ZOU, *Direct sampling method for diffusive optical tomography*, SIAM J. Sci. Comput., 37 (2015), pp. A1658–A1684.
- [15] Y.T. CHOW, K. ITO, AND J. ZOU, *A time-dependent direct sampling method for recovering moving potentials in heat equation*, SIAM J. Sci. Comput., 40 (2018), pp. A2720–A2748.
- [16] Y.T. CHOW, K. ITO, AND J. ZOU, *A direct sampling method for electrical impedance tomography*, Inverse Problems, 30 (2014), 095003, <https://doi.org/10.1088/0266-5611/30/9/095003>.
- [17] D. COLTON AND R. KRESS, *Inverse Acoustic and Electromagnetic Scattering Theory*, 3rd ed., Springer, Berlin, 2013.
- [18] J. DANCIGER, *A min-max theorem for complex symmetric matrices*, Linear Algebr. Appl., 412 (2006), pp. 22–29.
- [19] M. DING, J. LI, K. LIU, AND J. YANG, *Imaging of local rough surfaces by the linear sampling method with near-field data*, SIAM J. Imaging Sci., 10 (2017), pp. 1579–1602.
- [20] F. FOGLER, I. WALDSPURGER, AND A. D'ASPREMONT, *Phase retrieval for imaging problems*, Math. Program Comput., 8 (2016), pp. 311–335.
- [21] S. GARCIA, E. PRODAN, AND M. PUTINAR, *Mathematical and physical aspects of complex symmetric operators*, Inverse Problems, 47 (2014), 353001.
- [22] J. GARNIER AND G. PAPANICOLAOU, *Resolution analysis for imaging with noise*, Inverse Problems, 26 (2010), 074001.
- [23] S. HOU, K. SØLNA, AND H. ZHAO, *Imaging of location and geometry for extended targets using the response matrix*, J. Comput. Phys., 199 (2004), pp. 317–338.
- [24] K. ITO, B. JIN, AND J. ZOU, *A direct sampling method to an inverse medium scattering problem*, Inverse Problems, 28 (2012), 025003.
- [25] S. KANG, M. LAMBERT, AND W-K. PARK, *Direct sampling method for imaging small dielectric inhomogeneities: Analysis and improvement*, Inverse Problems, 34 (2018).
- [26] S. KANG, M. LAMBERT, AND W-K. PARK, *Multi-frequency direct sampling method in inverse scattering problem*, J. Phys. Conf. Ser., 904 (2017).
- [27] W-K. PARK, *A Novel Study on Direct Sampling Method for Imaging Multiple Targets*, DEStech Trans. Comput. Sci. Eng., 2017.

- [28] K. LIU, *A simple method for detecting scatterers in a stratified ocean waveguide*, Comput. Math. Appl., 76 (2018), pp. 1791–1802.
- [29] K. LIU, *Direct imaging of inhomogeneous obstacles in a three-layered ocean waveguide*, Commun. Comput. Phys., 26 (2019), pp. 700–718.
- [30] K. LIU, *Near-field imaging of inhomogeneities in a stratified ocean waveguide*, J. Comput. Phys., 398 (2019), 108901.
- [31] K. LIU AND J. ZOU, *A multilevel sampling algorithm for locating inhomogeneous media*, Inverse Problems, 29 (2013), 095003.
- [32] K. LIU, Y. XU, AND J. ZOU, *A multilevel sampling method for detecting sources in a stratified ocean waveguide*, J. Comput. Appl. Math., 309 (2017), pp. 95–110.
- [33] K. LIU, Y. XU, AND J. ZOU, *Direct recovery of wave-penetrable scatterers in a stratified ocean waveguide*, J. Comput. Appl. Math., 338 (2018), pp. 239–257.
- [34] G. WATSON, *Theory of Bessel Functions*, 2nd ed., Cambridge University Press, Cambridge, 1944.
- [35] J. YANG AND K. LIU, *Detecting buried wave-penetrable scatterers in a two-layered medium*, J. Comput. Appl. Math., 330 (2018), pp. 318–329.